Acta Geochim
https://doi.org/10.1007/s11631-020-00394-7

ORIGINAL ARTICLE

High oxygen fugacity magma: implication for the destruction of the North China Craton

Zhekun Zhang[1,5] · Mingxing Ling[3] · Lipeng Zhang[4] · Saijun Sun[4] · Weidong Sun[2,4,5]

Received: 16 December 2019 / Revised: 17 December 2019 / Accepted: 1 January 2020

Abstract The mechanism of lithospheric removal and destruction of the North China Craton (NCC) has been hotly debated for decades. It is now generally accepted that the subduction of the (Paleo)-Pacific plate played an important role in this process. However, how the plate subduction contributed to the craton destruction remains unclear. Here we report high oxygen fugacity (fO_2) characteristics of the Yunmengshan granite, e.g., hematite–magnetite intergrowth supported by zircon Ce^{4+}/Ce^{3+} ratios and apatite Mn oxygen fugacity indicator. High fO_2 magmas are widely discovered in Late Mesozoic (160–130 Ma) adakitic rocks in central NCC. The origin of high fO_2 magma is likely related to the input of the "oxidized mantle components", which shows a close connection between plate subduction and destruction of the craton. The research area is ~ 1500 km away from the current Pacific subduction zone. Considering the back-arc extension of Japan Sea since the Cretaceous, this distance may be shortened to ~ 800 km, which is still too far for normal plate subduction. Ridge subduction is the best candidate that was responsible for the large scale magmatism and the destruction of the NCC. Massive slab-derived fluids and/or melts were liberated into an overlying mantle wedge and modified the lithospheric mantle. Rollback of the subducting plate induced the large-scale upwelling of asthenospheric mantle and triggered the formation of extensive high fO_2 intraplate magmas.

Keywords High oxygen fugacity · Decratonization · North China Craton · Plate subduction

1 Introduction

North China Craton (NCC), one of the oldest cratons in the world, has shown similar characteristics to those of other cratons before the Middle Ordovician, i.e. having lasted for billions of years (Menzies et al. 1993, 2007). However, the ancient, thick (> 200 km) and cold heat flow (40 mW/m^2) cratonic mantle lithosphere was removed from the eastern NCC in the Paleozoic, and replaced by a young, thin (< 60 km) and high heat flow (80 mW/m^2) lithospheric mantle during the Mesozoic. It was accompanied by widespread intraplate magmatism and stretching deformation, suggesting destruction of the NCC (i.e. decratonization) (Fan and Menzies 1992; Gao et al. 2004; Menzies et al. 2007; Niu 2005; Wu et al. 2002, 2005a; Xu 2001; Xu et al. 2004; Yang et al. 2008; Zhang et al. 2002, 2003, 2007; Zhu et al. 2011, 2012). There are currently several models for the destruction of the NCC, e.g., delamination of the eclogitic lower continental crust (LCC)

Electronic supplementary material The online version of this article (https://doi.org/10.1007/s11631-020-00394-7) contains supplementary material, which is available to authorized users.

✉ Mingxing Ling
mxling@gig.ac.cn

1 CAS Key Laboratory of Mineralogy and Metallogeny, Guangzhou Institute of Geochemistry, Chinese Academy of Sciences, Guangzhou 510640, China

2 Laboratory for Marine Mineral Resources, Qingdao National Laboratory for Marine Science and Technology, Qingdao 266237, China

3 State Key Laboratory of Isotope Geochemistry, Guangzhou Institute of Geochemistry, Chinese Academy of Sciences, Guangzhou 510640, China

4 Center of Deep Sea Research, Institute of Oceanology, Chinese Academy of Sciences, Qingdao 266071, China

5 University of Chinese Academy of Sciences, Beijing 100094, China

Published online: 08 January 2020

(Gao et al. 2004; Wu et al. 2002), thermal/chemical erosion of the lithospheric mantle (Menzies et al. 2007; Xu 2001; Zhang et al. 2003), decratonization triggered by subducted Triassic slab and continued in the Cretaceous (Yang et al. 2008; Zhao et al. 2016), hydration induced by Pacific Plate subduction (Niu 2005), the rollback of subducted flat slabs and melt–peridotite reactions (Kusky et al. 2014), slab rollback-induced unstable mantle flows (Zhu et al. 2011), the destruction induced by ridge subduction (Ling et al. 2013; Wu et al. 2017). Anyhow, there is increasing evidence that the subduction of the (Paleo)-Pacific plate played a key role in the destruction of NCC (Ling et al. 2013; Niu 2005; Wu et al. 2005a, b; Zhu et al. 2011, 2012).

Oxygen fugacity is an intrinsic thermodynamic property that records the chemical activity of oxygen and controls the speciation of redox-sensitive elements in the solid Earth. More attentions have been paid to it in recent years, including the origin of high fO_2 in arc magmas, oxidized magmas associated with of porphyry Cu–Au–Mo deposits (Kelley and Cottrell 2009, 2012; Lee et al. 2005, 2010; Sun et al. 2013, 2015, 2016). The fO_2 of intraplate settings, including abyssal peridotite, mid-ocean ridge basalt (MORB) and continental peridotite fall between ΔFMQ $-$ 3 and 0 log units, whereas the fO_2 of subduction settings (arc magmas) range between ΔFMQ 0 and $+$ 3, indicating that intraplate magmas without influences from plate subduction are considerably reduced (Frost and McCammon 2008; Sun et al. 2013).

Here we report Late Mesozoic rocks in central NCC that are characterized by high fO_2. The research area is distributed in central NCC and is $\sim$ 1500 km away from the current Pacific subduction zone (Fig. 1). Generally, oxidized magmas are mainly distributed in subduction zones, why do these intraplate rocks show high fO_2 characteristics, and what was the mechanism of forming such large volumes of high fO_2 magmas? In this contribution, we present detailed studies on Yunmengshan and Fangshan batholiths, NCC. This together with a compilation of literature data indicate that high fO_2 characteristics of Late Mesozoic plutons in NCC may be widespread. This study aims to explore: (1) whether massive slab-derived material entered into the depth and recycled to the crust? (2) what is the redox state of the big mantle wedge beneath the eastern NCC? It may provide new insight on understanding the process of magma mixing, crust-mantle interaction, and the destruction of NCC.

2 Geological background and samples

The NCC formed in the Paleoproterozoic by the assembly of two Archean blocks, the Eastern and Western blocks, along the Trans-North China orogen (Zhao et al. 2001). The basement consists primarily of the Early to Late Archean (3.8–3.0 Ga) TTG (tonalite-trondhjemite-granodiorite) gneisses and $\sim$ 2.5 Ga granitoids (Liu et al. 1992). Subsequently, the NCC has been stable for $\sim$ 2.0 Ga and is covered by thick Proterozoic to Paleozoic sequence. Large-scale magmatic activities and metamorphic core complexes occurred in the NCC during the Late Mesozoic, indicating the reactivation of an ancient craton (Fan and Menzies 1992; Gao et al. 2004; Wu et al. 2005a, b; Yang et al. 2008; Zhu et al. 2011). Geochronological studies indicate that the magmatic rocks mostly formed in the Late Jurassic (180–150 Ma) and Early Cretaceous (135–117 Ma) (Wu et al. 2005a, b). Among them, the Early Cretaceous magmatism is the strongest. Researches indicated that those rocks were mainly derived from partial melting of ancient continental crustal materials with the addition of mantle materials via magma mixing (Sun et al. 2010; Wu et al. 2005a).

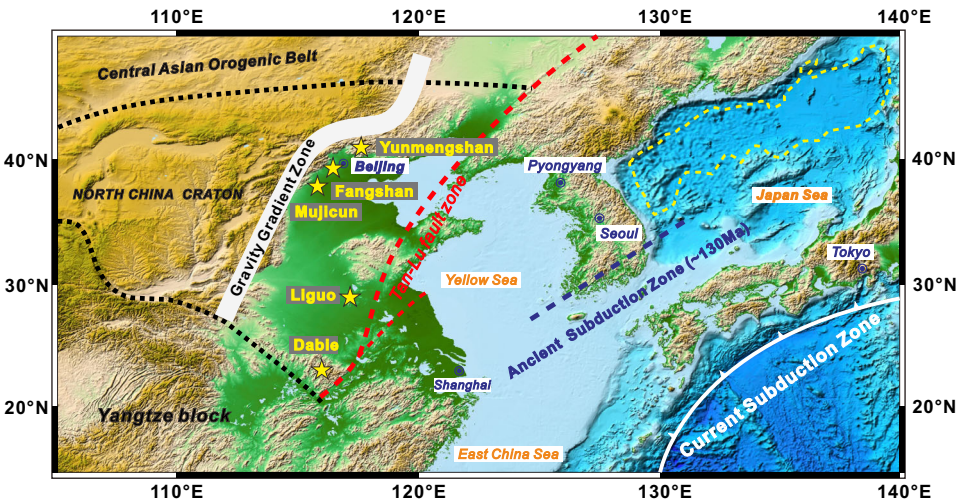

Fig. 1 Regional map showing the location of the study area. Color shows the surface topography. Yellow star show the distribution of our samples and literature data. Yellow dotted line show the position of Japan island arc during the early Cretaceous ($\sim$ 130 Ma), and the blue dotted line show the location of ancient subduction zone

In this study, we selected four famous batholiths in central NCC. The Yunmengshan batholith (Fig. 2a) is located north of Beijing in the Yanshan Fold and Thrust Belt (YFTB). The batholith is an NNE-elongate intrusion and is 25 km long and 12 km wide (with a total area of ~ 270 km^2). The Yunmengshan batholith contains Yunmengshan (YMS) granite and Shicheng (SC) monzodiorite intruding into the Archean-Paleoproterozoic metamorphic basement (Davis et al. 1996). The granite is medium-fine grained. The mineral assemblage consists of plagioclase (~ 30%), alkali-feldspar (~ 25%), quartz (~ 25%), biotite (~ 15%), and hornblende (2%). Accessory minerals include apatite, zircon, titanite, and Fe–Ti oxides. A mylonitic texture is commonly developed parallel to the boundary between granite and host rocks. Zircon U–Pb ages are 141–144 Ma (Davis et al. 2001; Wang et al. 2012; Zhao and Wang 2014; Zhu et al. 2015). Monzodiorite is distributed in the northeast corner of the batholith. The mineral assemblage consists of plagioclase (~ 55%), quartz (~ 5%), biotite (~ 25%), hornblende (10%), and pyroxene (~ 5%). Accessory minerals include apatite, zircon, titanite and Fe–Ti oxides. Zircon U–Pb dating revealed that the pluton intruded in 150–156 Ma.

The Fangshan pluton (Fig. 2b) is located to the southwest of Beijing in the YFTB, and intruded into Archean gneiss, with an outer annulus of quartz diorite surrounding a central core of granodiorite with abundant mafic microgranular enclaves (MME) and mafic dyke. Previous U–Pb dating yielded formation ages of 129–134 Ma for the porphyritic core and 130–134 Ma for the outer annulus quartz diorite, the ~ 134 Ma for MME and ~ 134 Ma for mafic dyke (Sun et al. 2010; Xu et al. 2012). The fine-grained quartz diorites are mainly composed of fine-grained plagioclase (40–45%), K-feldspar (25–30%), quartz (~ 10%) and amphibole (10–15%), with a minor amount (< 5%) of apatite, zircon, titanite and Fe–Ti oxides. The granodiorite is composed of plagioclase (45–50%), alkali-feldspar (15–20%), quartz (20–25%), biotite (5%) and hornblende (5–10%). Accessory minerals include apatite, zircon, titanite and Fe–Ti oxides. The mafic enclaves are mainly dioritic in composition, containing plagioclase (45–55%), hornblende (30–35%), biotite (5–10%), and small amounts of quartz, K-feldspar, pyroxene, and accessory titanomagnetite, titanite, apatite and zircon. The mafic dyke swarms are about 2–3 km long and 0.1–3 m wide, including some fresh diabases, gabbros, and diorites.

The Dabie Orogen is extensively distributed by large-scale Cretaceous (143–129 Ma) granitic and minor mafic–ultramafic intrusions (130–123 Ma). The Tiantangzhai

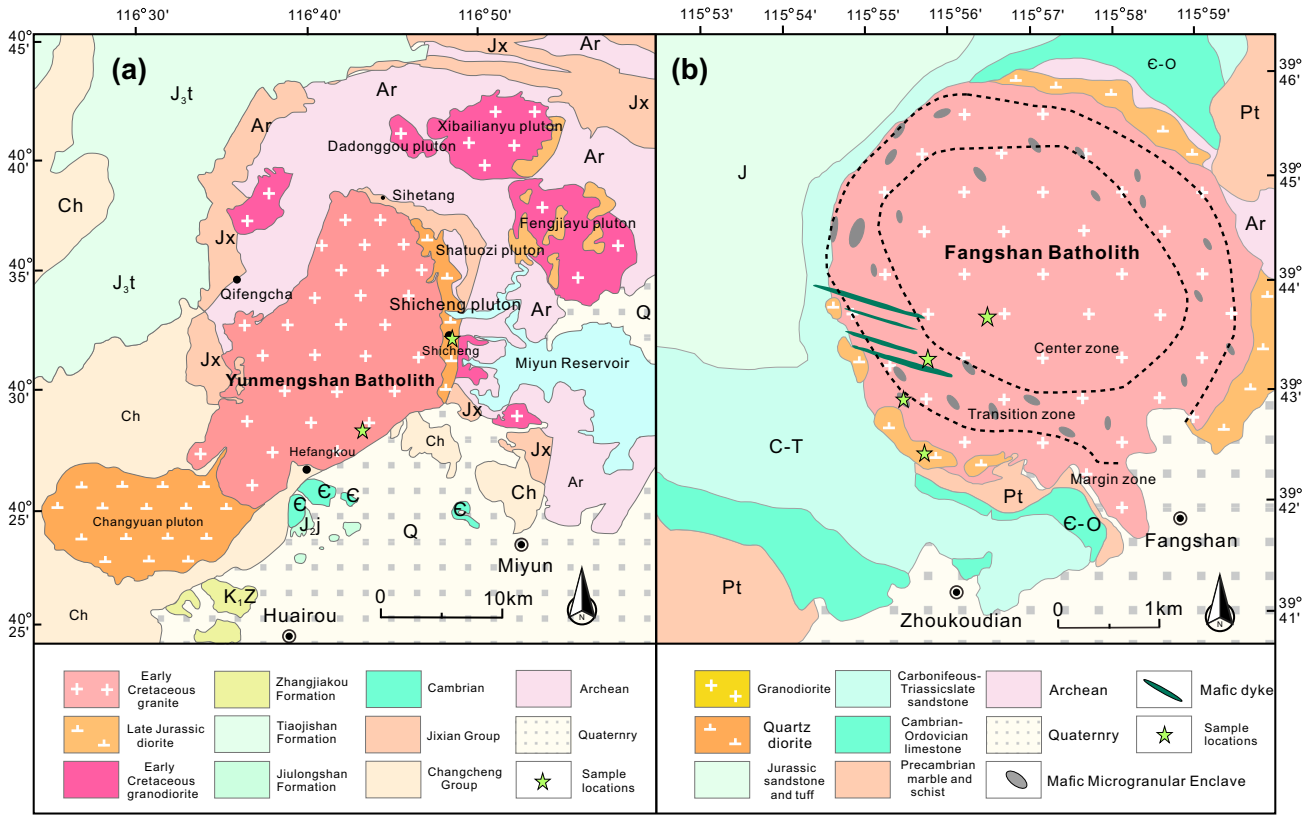

Fig. 2 **a** Simplified geological map of the Yunmengshan batholith (modified after Zhu et al. 2015). **b** Simplified geological map of the Fangshan batholith (modified after Xu et al. 2012)

(TTZ) intrusion is the biggest of the early granites with an outcrop area of more than 400 km^2 and is characterized by the high Sr/Y and $(La/Yb)_N$ ratios, showing characteristics of adakitic rocks. Previous researches have shown that the granites plausibly originated from the thickened LCC (> 40–50 km) (Ling et al. 2011; Liu et al. 2010; Wang et al. 2007). The Liguo (LG) intrusive in the Xu-Huai region, consisting of granodiorites and hornblende diorites, were formed in Early Cretaceous (~ 130 Ma). Liguo pluton has high SiO_2 (64–71.6 wt%), high Sr (502–655 ppm), low Y (3.0–9.1 ppm), with high Sr/Y ratios (55.9–178.3), and $(La/Yb)_N$ ratios. The rocks contained abundant inherited zircon (~ 2.5 Ga), corresponding to the age of the NCC basement. Previous studies have shown that those rocks were derived from the partial melting of subduction oceanic crust (Sun et al. 2019).

3 Methods

3.1 Whole-rock major and trace elements analyses

The major elements of the bulk rock samples were analyzed at the State Key Laboratory of Isotope Geochemistry, Guangzhou Institute of Geochemistry, Chinese Academy of Sciences (GIGCAS). The bulk rock major elements were conducted using X-ray fluorescence spectrometry (Rigaku 100e) with analytical precisions better than 1%. The trace element analysis of the whole rock was conducted on an Agilent 7700e ICP-MS at the Wuhan Sample Solution Analytical Technology Co. Ltd. Wuhan, China (Sun et al. 2018a).

The whole rocks Fe^{2+} (FeO wt%) contents were analyzed by redox titrations. Firstly, the samples were dissolved in sulfuric acid and hydrofluoric acid. Secondly, the sample solutions were transferred to dilute sulfuric acid. Finally, titration is done with potassium dichromate. This analysis was done in ALS Chemex Laboratories (Guangzhou). The detection limit of FeO is 0.01–100%. All results of major and trace element analyses for the Yunmengshan and Fangshan plutons are listed in Tables S1 and S2.

3.2 Trace element analysis of zircon

Fresh samples were broken into small pieces, then washed and crushed to 200-mesh for zircon separation. Trace element of zircon was obtained using Agilent 7900 ICP-MS coupled with a Resonetics RESOlustion S-155 ArF 193 nm laser-ablation system at the Key Laboratory of Mineralogy and Metallogeny, GIGCAS. A laser spot of 29 μm in diameter was operated with an energy density and a repetition frequency of 8 Hz. The NIST SRM 610 glass and TEMORA were used as an external standard and ^{91}Zr as an internal standard for trace elements analyses (Sun et al. 2018b). The calculations of zircon isotope ratios and zircon trace elements were performed by ICPMSDataCal 8.3 (Liu et al. 2008). All the results are listed in Table S3.

3.3 Zircon Ce^{4+}/Ce^{3+} ratio

Zircon is a common accessory mineral in most intermediate to felsic igneous rocks and is resistant to post crystallization disturbances. Zircon partitions Ce^{4+} in strong preference to Ce^{3+}, which means the Ce^{4+}/Ce^{3+} ratio can be a sensitive indicator of magma oxygen fugacities. Zircon-melt partition coefficients for Ce^{3+} and Ce^{4+} are estimated using the lattice strain model (Blundy and Wood 1994):

$$lnD_i = lnD_O - \frac{4\pi EN_A}{RT}\left(\frac{r_i}{3} + \frac{r_o}{3}\right)(r_i - r_o)^2$$

where $D_i = D_{zircon/rock}$. The zircon Ce^{4+}/Ce^{3+} ratios are estimated using the equation (Ballard et al. 2002; Liang et al. 2006).

$$\left(\frac{Ce^{4+}}{Ce^{3+}}\right)_{zircon} = \frac{Ce_{melt} - \frac{Ce_{zircon}}{D_{Ce^{3+}}}}{\frac{Ce_{zircon}}{D_{Ce^{4+}}} - Ce_{melt}}.$$

Whole rock trace element data and zircon trace elements combined with zircon-melt partition coefficients for Ce^{3+} and Ce^{4+} are used to calculate the zircon Ce^{4+}/Ce^{3+} ratio. The standard error of the Ce^{4+}/Ce^{3+} ratio is from the linear fitting between trace element partition coefficients of zircon and whole rock ($D_{zircon/rock}$) and ionic radius. In this study, the error of the zircon Ce^{4+}/Ce^{3+} ratio is less than 35 (Zhang et al. 2013, 2017). There are some differences between the method described by Ballard et al. (2002) and Zhang et al. (2017). Zhang et al. (2017) exclude REEs such as La, Pr, and Eu for Ce^{3+} estimation, and also the tetravalent cation U for Ce^{4+} estimation because of the low concentrations of LREEs cannot be accurately measured, and also can be disturbed by inclusions. In this study, we stick to the method of Zhang et al. (2017) to calculate zircon Ce^{4+}/Ce^{3+} ratios. The results are listed in Table S3. The area of ore barren and ore-bearing rocks in Chile is from Ballard et al. (2002); the area of ore-bearing rocks in Dexing is from Zhang et al. (2013, 2017).

3.4 EMPA analysis of apatite

Major element compositions of apatite grains in situ were analyzed using a JEOL JXA 8230 electron microprobe (EMPA) at the Key Laboratory of Mineralogy and Metallogeny, GIGCAS. The operating conditions were as

follows: 15 kV accelerating voltage, 20 nA beam current, and 3 μm beam diameter. The results are listed in Table S4.

3.5 Oxygen fugacity estimation by apatite

Apatite is an important accessory mineral widely grew in intermediate and silicic igneous rocks. Research showed that the Mn content of apatite seems to be largely independent of Mn concentration in the melt, and there is an apparent negative correlation between the oxygen fugacities of magma and Mn concentrations in apatite from a range of intermediate to silicic volcanic rocks (Miles et al. 2014), such that:

$$logfO_2 = -0.0022(\pm 0.0003)Mn(ppm) - 9.75(\pm 0.46).$$

Therefore we can estimate oxygen fugacities by Mn concentration of apatite.

ΔFMQ = log fO_2 (sample) − log fO_2 (FMQ buffer), and the log fO_2 (sample) were estimated based on compositions of apatite (Miles et al. 2014), and FMQ (fayalite-magnetite-quartz buffer curve) referenced to O'Neill (1987). The apatite saturation temperatures were obtained using the methods of Harrison and Watson (1984).

4 Results

Magnetite—hematite intergrowths are commonly found in YMS granite (Fig. 3). The samples are fresh without weathering and mineralization, and some magnetite and hematite grains are included in other rock-forming minerals (e.g., feldspar), suggesting very high fO_2 of the magmas.

The samples of YMS and FS batholiths range from diorite to granite (52–75 wt.% SiO_2), and both show the higher bulk rock $Fe^{3+}/\Sigma Fe$ ratios (between 0.3 and 0.6). The $Fe^{3+}/\Sigma Fe$ of low silica ($SiO_2 < 65$ wt.%) samples of Dabie are consistent with YMS and FS, but the high SiO_2 samples show the low ratios (between 0.1 and 0.3) (Fig. 4a, Table S1). Compared with MORB, all the samples show high fO_2.

The majority of zircons Ce^{4+}/Ce^{3+} and Eu/Eu* ratios are mostly in the range of 100–1000, and consistent with ore-bearing porphyries in Chile and China (e.g., Dexing) (Zhang et al. 2017), indicating the high fO_2. Conversely, the inherited zircon ($\sim$ 2.5 Ga) Ce^{4+}/Ce^{3+} ratios of Liguo and FS plutons range from 10 to 200, similar to those of ore barren porphyries in Chile, i.e. low fO_2 (Fig. 5a, Table. S3).

The fO_2 of YMS and FS batholiths was estimated by apatite, as shown in Fig. 6 and Table S4. The fO_2 of SC monzodiorite ranges from ΔFMQ + 3 to ΔFMQ + 4, and the fO_2 of the enclaves contained in FS pluton ranges from ΔFMQ + 1.5 to ΔFMQ + 2.5, showing very high fO_2 characteristics. However, compared with the low silicon rocks ($SiO_2 < 60$ wt.%), the YMS granite and FS granodiorite show relatively low fO_2.

5 Discussion

5.1 High oxygen fugacity magma of the NCC

The Fe–Ti oxides are important accessory minerals of granitic rocks, their abundance and proportions mainly depend on temperature (T) and fO_2 of the magma (Krishnamurthy 2015). Primary hematite in close association with magnetite of the samples in this study (Fig. 3) strongly suggests very high fO_2, reaching the magnetite-hematite buffer, which is about ΔFMQ + 4 (Sun et al. 2013, 2015). The detailed study of the fO_2 from our samples and literature data, including zircon Ce^{4+}/Ce^{3+}, and fO_2 estimated by apatite and the whole rock $Fe^{3+}/\Sigma Fe$ ratios (Figs. 3, 4, 5, 6) indicate that these rocks have very high fO_2.

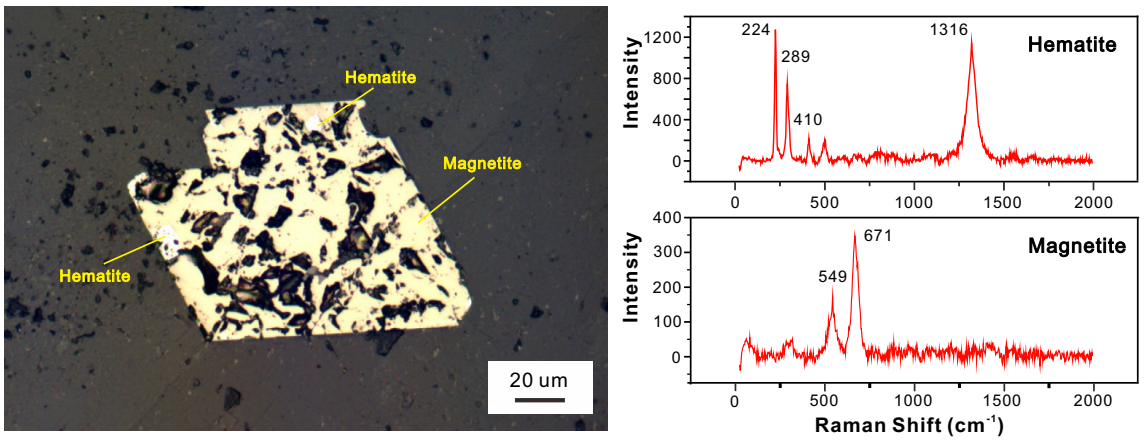

Fig. 3 Reflected light microphotographs and Raman spectra of hematite and magnetite intergrowths from YMS granite

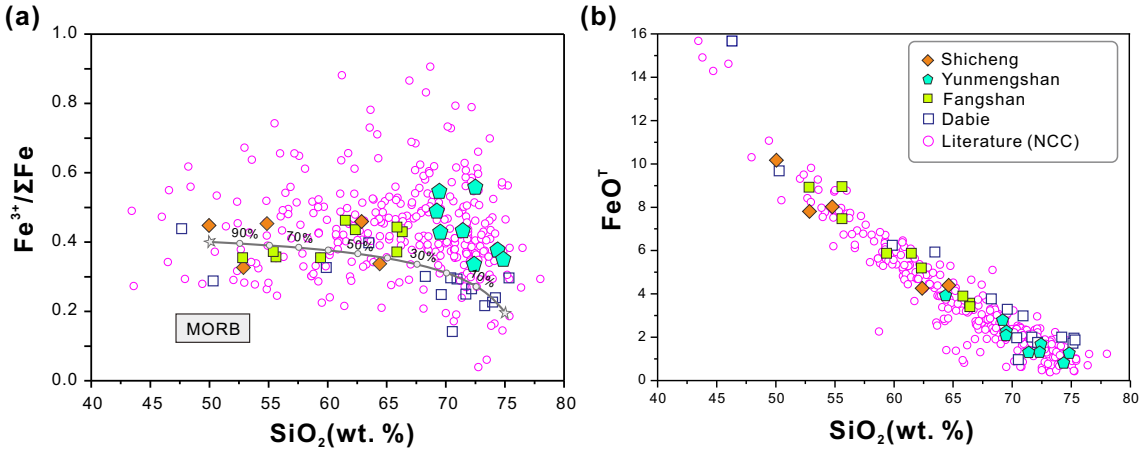

Fig. 4 **a** Compiled $Fe^{3+}/\Sigma Fe$ ratios plotted as function of SiO_2. The data of MORB is after Cottrell and Kelley (2011). **b** The FeO^T (wt.%) versus SiO_2 diagram. The red circle (n > 400) are data in NCC from published literatures and GEOROC

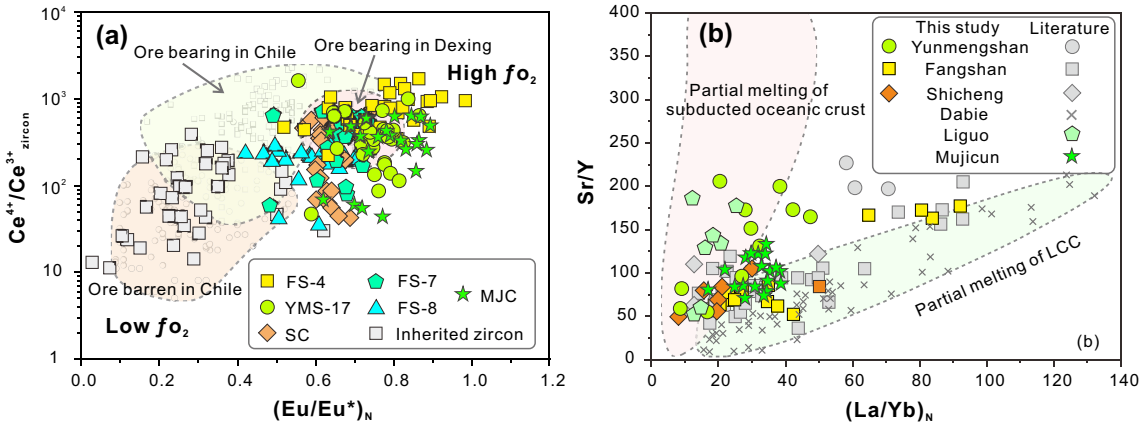

Fig. 5 **a** Zircon Ce^{4+}/Ce^{3+} ratios versus Eu anomalies diagrams for intrusive rocks of NCC. The area of ore barren and ore bearing rocks in Chile is from Ballard et al. (2002); the area of ore bearing rocks in Dexing from Zhang et al. (2017) and Zhang et al. (2013). **b** Sr/Y versus $(La/Yb)_N$ diagram discriminating adakites of different origin, after Ling et al. (2013) and Liu et al. (2010). The $(Eu/Eu^*)_N$ ratios and $(La/Yb)_N$ are chondrite normalized values (Sun and McDonough 1989). The Mujicun deposit is a large porphyry type Cu–Mo deposit, after Gao et al. (2012). More detailed data is provided in the appendix: supplementary data S5

Furthermore, data compilation of > 40 plutons in the NCC show $Fe^{3+}/\Sigma Fe$ ratios ranging from 0.3 to 0.6 (Fig. 4a), indicating that the high fO_2 characteristics in the NCC during the Late Mesozoic may be widespread.

Convergent margins (arc magmas) have higher fO_2 compared to intraplate settings (Brounce et al. 2015; Frost and McCammon 2008; Grocke et al. 2016; Kelley and Cottrell 2009; Sun et al. 2013). However, the origin of high fO_2 arc magmas has been hotly debated (Kelley and Cottrell 2009, 2012; Lee et al. 2005, 2010). It has been proposed that the mantle wedge above the subduction zone is apparently more oxidized as a result of metasomatism by slab-derived fluid and/or melt (Brounce et al. 2015; Kelley and Cottrell 2009). Lee et al. (2010) argued that the redox state of initial arc magmas is not significantly distinguishable from those of MORB, and high fO_2 of arc magma may result from shallow-level magma differentiation processes.

We compiled the whole-rocks major compositions from more than 40 adakitic rocks (nearly 400 data) from NCC. In the plot of $Fe^{3+}/\Sigma Fe$ and FeO^T versus SiO_2, FeO^T decreases while SiO_2 increases, indicating the magma differentiation process, which is not shown by $Fe^{3+}/\Sigma Fe$ (Fig. 4). Only when the SiO_2 content rises above ~ 68 wt.%, the $Fe^{3+}/\Sigma Fe$ ratios slightly decrease, which may be the result of magnetite separation. This is well supported by Grocke et al. (2016), in which the samples from Tequila (Mexico) and Pinatubo (Philippines) show an insignificant change in $Fe^{3+}/\Sigma Fe$ ratios from basalt to rhyolite. Hence, we propose that the impacts of the shallow-level magma differentiation processes on the fO_2 of our samples may be insignificant.

Many inherited zircons (~ 2.5 Ga) are present in FS and Liguo plutons, and the zircon Ce^{4+}/Ce^{3+}ratios and Eu/Eu* are very low. This is consistent with ore barren

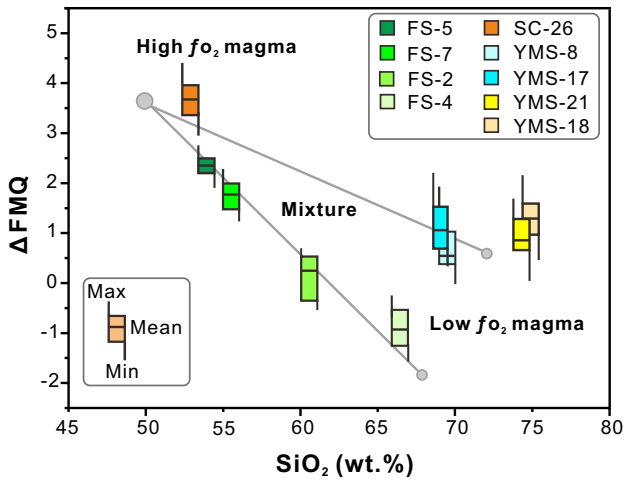

Fig. 6 ΔFMQ versus silica content of whole rock diagrams. Where ΔFMQ = log fO_2 (sample) − log fO_2 (FMQ buffer), and the log fO_2 (sample) were estimated based on compositions of apatite (Miles et al. 2014), and FMQ (fayalite-magnetite-quartz buffer curve) referenced to (O'Neill 1987)

porphyries in Chile, showing low fO_2 (Fig. 5). In addition, the $Fe^{3+}/\Sigma Fe$ ratios of adakitic rocks ($SiO_2 > 65$ wt.%) from Dabie is far lower than the YMS and FS plutons (Fig. 4a), also revealing the relatively low fO_2. Previous studies have shown the Dabie adakitic rocks originated from the partial melting of thickened LCC (Fig. 5b) (Ling et al. 2013; Liu et al. 2010). Thus, the ancient Archean basement is likely to be reductive, and the high fO_2 characteristics of YMS and FS should not inherit from the partial melting of LCC or the contamination of the surrounding rocks.

Yunmengshan granite and FS granodiorite are characterized by the high Sr/Y (65–200) and $(La/Yb)_N$ (20–100) ratios, old TDM_2 (Hf) model age (~ 2.5 Ga). Using the discrimination diagram of adakites, if the adakites originated from partial melting of LCC (e.g. Dabie complex), the slope of $(Sr/Y)/(La/Yb)_N$ is very low, but many samples of YMS and FS deviate from the region (partial melting of LCC) and are close to the region of slab melting (Fig. 5b), indicating that magmas mixed with some subduction related material (Ling et al. 2013; Liu et al. 2010). The oxygen fugacity estimated by apatite also show well mixture characteristics (Fig. 6) such as FS pluton. The enclaves show the high fO_2, the granodiorite shows the low fO_2, and the quartz diorite show the medium fO_2, revealing the characteristic of a mixture of two components. Similarly, the YMS pluton shows the high fO_2 as a result of the input of mafic melts. On the contrary, the adakitic rocks of Dabie show the low fO_2 without the contamination of "mantle component". In addition, Late Mesozoic granitoids contains abundant MMEs and mafic dykes, widely distributed in central NCC, which are important markers of mafic magma underplating and crust-mantle interaction. Therefore, the origin of high fO_2 is more possibly related to the addition of "mantle components".

Iron is an element with variable valences and sensitive to redox reaction. Which also has very high abundances in the Earth, iron-bearing minerals are the important oxygen fugacity buffer, controlling the change of fO_2 in different geological processes. So the whole rocks $Fe^{3+}/\Sigma Fe$ can usually be used to indicate the redox state of magma.

In order to understand how much of the impact can the mafic magma adds into the felsic magma, we perform a simulation calculation. We ignored the effect on fO_2 of other factors (including magmatic degassing and differentiation). Underplating basic magma was selected as a mafic member, we presumed the primary composition of melt, the SiO_2 (~ 50 wt.%), $Fe^{3+}/\Sigma Fe$ (0.4), and the FeO^T (10 wt.%). The high silicon adakitic rocks were selected as felsic members. We also presumed the composition, the SiO_2 (~ 75 wt.%), $Fe^{3+}/\Sigma Fe$ (0.20), and the FeO^T (2 wt.%). Mixing results of the two members with different proportions are shown in Fig. 4a. Only if the 10% mafic magma was added into felsic magma was the change of $Fe^{3+}/\Sigma Fe$ ratios more than 0.07. Obviously, the mixing ratios are more than 10% in nature. Therefore, we believe the Late Mesozoic large-scale underplating of basic magma may be the important factor that increases the fO_2 of adakitic rocks.

5.2 Subduction of the (Paleo)-Pacific plate and an oxidized big mantle wedge

The increasing evidence studies show that the NCC experienced continuous subduction of the (Paleo)-Pacific plate from Jurassic (~ 170 Ma) (Wu et al. 2005a, b), then the rollback of the subducting plate during Early Cretaceous (~ 130 Ma) (Fig. 7) (Ling et al. 2013; Sun et al. 2007; Wu et al. 2005a, b; Zhu et al. 2012). However, we know very little about the link between the subduction plate and the deep mantle under NCC.

Plate tectonics drives the recycling of surface material into the Earth's interior, introducing hydrated and oxidized oceanic lithosphere into the mantle at subduction zones (Evans 2012; Evans et al. 2017). Fluids liberated during dehydration of subducted crust trigger partial melting of the overlying mantle leading to the formation of volcanic arcs, dominated by oxidized rocks (Ballhaus 1993). The enrichment of LILE and the strong depletion of HFSE are generally taken as significant characteristics of arc magmas (Kelemen et al. 2003). A lot of alkali basalts erupted in Eastern China during Late Mesozoic, including Fangcheng, Feixian, Chengde, Jinling, Fuxin, Qujiatun, Laohutai, etc. (Zhang et al. 2003). There is a geochemical contrast between > 108 Ma and < 108 Ma basalts (Wu et al. 2017).

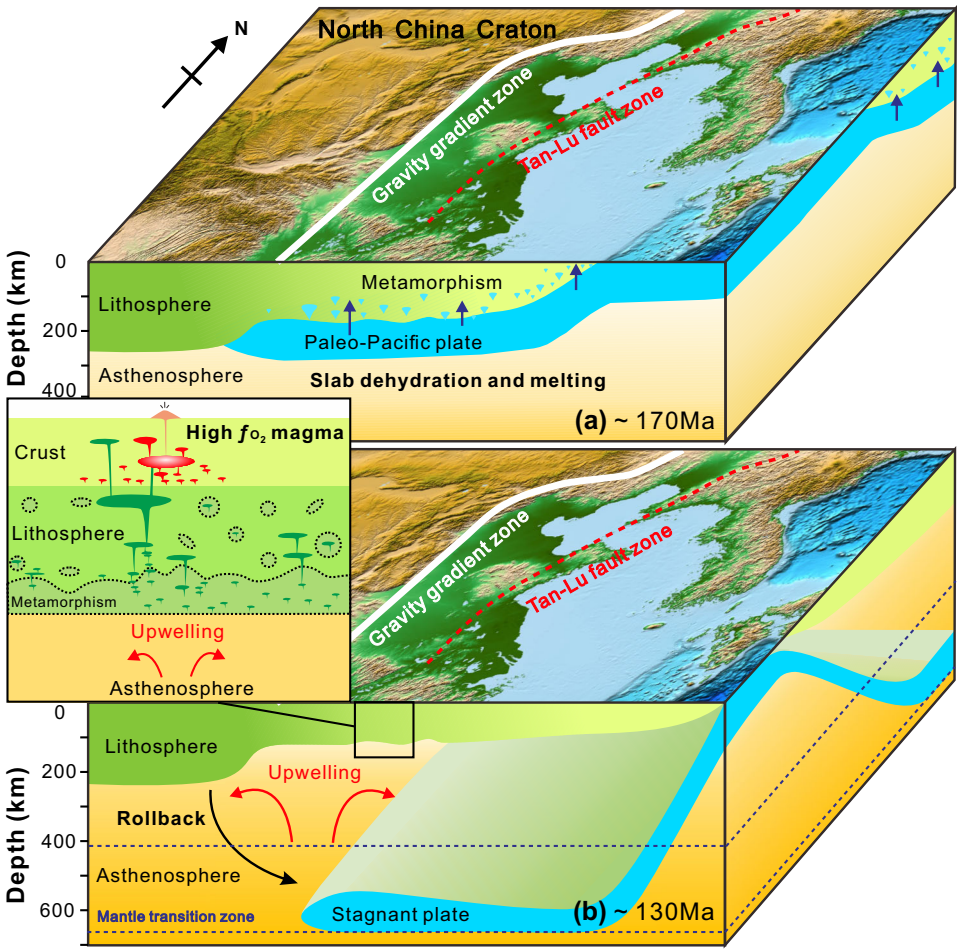

Fig. 7 **a** The subduction of Paleo-Pacific may have started in the Early Jurassic. Northwestward flat subductions started in the Late Jurassic to Early Cretaceous, which may have reached the inner land and was responsible to the destruction of the North China Craton (Ling et al. 2009, 2013). Much slab-derived fluid and/or melt releases into overlying mantle wedge. **b** The rollback of the (Paleo)-Pacific plate, resulted in upwelling of asthenospheric mantle, and triggered the formation of large-scale high fO_2 intraplate magmas

The < 108 Ma alkali basalts are characterized by oceanic island basalts (OIB)-like geochemical compositions. However, the > 108 Ma alkali basalts are an enrichment of much fluid mobile elements and depletion of HFSE, showing arc-like features. The flux of fluid mobile elements of alkali basalts show a close link with the (Paleo)-Pacific plate drift direction (Wu et al. 2017). Previous researches discovered that the water content (> 1000 ppm) of lithospheric mantle source beneath NCC (~ 120 Ma) is much higher than other cratons, and the water content of primitive basaltic magma can even reach the level of modern island arc basalts (Xia et al. 2013). In addition, the $\delta^{18}O$ values of clinopyroxene in the OIB-type mafic rocks in the east NCC, are dominantly higher than that of the clinopyroxene from normal MORB (5.4–5.8 ‰), which confirms the role of recycled oceanic crust in their mantle sources (Liu et al. 2017). The Liguo pluton shows adakitic characteristi and high oxygen fugacity, and contains high F and Cl contents (Sun et al. 2019). All these indicate that the ancient lithospheric mantle in eastern China may be significant modified by the subducted slab during the Late Mesozoic.

Oceanic sediments may contain $Fe^{3+}/\sum Fe$ ratios up to 0.82 and altered basalts up to 0.19–0.24 (Lécuyer and Ricard 1999). The subducting oceanic lithospheric mantle may also become oxidized through the formation of serpentine and brucite, which release Fe from their olivine that then forms magnetite (and H^+, which escapes the system) at the expense of H_2O (Berndt 1996). That excess Fe^{3+} could be transported directly from the slab into the mantle wedge by dissolving in hypersaline brines, supercritical fluids, or silicate melts (Kelley and Cottrell 2012). Recent research has shown that the oxidized materials (including sulfur and carbon) carried by the subduction plate may be very important, which could oxidize the mantle wedge of subduction zones without requiring direct transport of Fe^{3+}. More Fe^{2+} is oxidized to form Fe^{3+} by sulfur and carbon reduction in the mantle wedge beneath arc (Evans 2012; Rielli et al. 2017). Brounce et al. (2015) reported that fO_2 of the mantle wedge in Mariana was raised by ~ 1.3 orders of magnitude as the addition of oxidizing slab fluids, reaching conditions essentially equivalent to the modern arc in just 2–4 Ma. The NCC suffered nearly 50 Ma of subduction, we propose that the mantle wedge beneath NCC gradually become oxidizing with the input of oxidized fluids and/or melts. This is also well supported by abundant water of the mantle wedge beneath NCC in the Late Mesozoic.

5.3 Geodynamic implications

The research area is ~ 1500 km away from current subduction zones, however, the high fO_2 characteristics were inherited from oxidized mantle sources. This is too far even for flat subduction (Fig. 1). The reconstruction of tectonic evolution history of the Japan Sea, show that the distance of back-arc spreading are over ~ 700 km since the Cretaceous (Jolivet et al. 1994), we restore the Japan island arc to its original position and find that the ancient subduction zone (~ 130 Ma) close to the south edge of the Korean peninsula. This distance may be shortened to 800 km, which is still too far for normal plate subduction. However, this is within the distance of flat plate subduction during ridge subduction (Ling et al. 2009, 2013; Wu et al. 2017). In addition, high-resolution mantle tomography of NCC revealed the Pacific slab is stagnant in the mantle transition zone under eastern China, and the western edge of the stagnant slab is roughly coincident with eastern of the gravity gradient zone (Fig. 7) (Zhao et al. 2007). Previous studies have confirmed that flat-lying slabs in the mantle transition zone are generated largely by the rollback of the subduction zone, not lateral penetration of the slabs, and dehydration reactions from slabs can significantly hydrate the overlying mantle (Kusky et al. 2014).

This model also offers a good explanation for the high fO_2 intraplate magmas. During the northwestward plate subduction, slab-released fluids and/or melts continuous modified the overlying mantle wedge (Fig. 7a), and then the rollback of subducting Pacific plate, resulting in back-arc extension and the upwelling of convective asthenosphere mantle, which have triggered the large-scale partial melting of the metasomatized mantle and thickened LCC, the high fO_2 mafic melts that mixed with those melts derived from LCC (Fig. 7b).

Widespread Late Mesozoic high fO_2 granitoids formed by partial melting of ancient low crust, with significant input of the oxidized mantle component via magma mixing. This is associated with the removal of lithospheric and the destruction of NCC. The ridge subduction of the Pacific and Izanagi plates have significant influence on this process, including the following aspects: (1) the flat subduction during ridge subduction resulted in intense physical erosion on the thick lithosphere root (Ling et al. 2013); (2) voluminous slab-released fluid and/or melt weakened the strength of lithosphere mantle (Niu 2005; Wu et al. 2017); (3) the rollback of the flat plate strongly disturbed asthenosphere, resulting in large scale magmatism. Moreover, the timing and scale of destruction of the NCC are also highly consistent with the ridge subduction. We propose that ridge subduction in the Late Mesozoic was responsible for the destruction of the NCC.

6 Conclusions

That adakitic rocks with high oxygen fugacity are very widespread in the NCC. Those magmas were derived from partial melting of thickened lower continental crust with the mixing of mantle materials, and the high fO_2 characteristic inherited from an oxidized mantle source that has been modified by fluids and/or melt derived from (Paleo)-Pacific plate. The research of magmas fO_2 provides new insight into understanding the process of magma mixing and the crust-mantle interaction in NCC during the Late Mesozoic. Ridge subduction provides a good explanation for such high oxygen fugacity. These results also support that ridge subduction was the main control factor that induced the destruction of the NCC.

Acknowledgements This study was supported by National Key R&D Program of China (2016YFC0600408), Strategic Priority Research Program (B) of the Chinese Academy of Sciences (XDB18020102), Guangdong Natural Science Funds (2014A030306032 and 2015TQ01Z611), and Youth Innovation Promotion Association CAS (2016315). We thank Drs. Rongqing Zhang and Liuyi Zhang for their assistance of field work. No. IS-2794 from GIGCAS has a contribution in this work.

References

Ballard JR, Palin MJ, Campbell IH (2002) Relative oxidation states of magmas inferred from Ce(IV)/Ce(III) in zircon: application to porphyry copper deposits of northern Chile. Contrib Mineral Petrol 144:347–364

Ballhaus C (1993) Redox states of lithospheric and asthenospheric upper mantle. Contrib Miner Petrol 114:331–348. https://doi.org/10.1007/BF01046536

Berndt ME (1996) Reduction of CO_2 during serpentinization of olivine at 300 °C and 500 bar. Geology 24:351–354

Blundy J, Wood B (1994) Prediction of crystal–melt partition coefficients from elastic moduli. Nature 372:452–454

Brounce M, Kelley KA, Cottrell E, Reagan MK (2015) Temporal evolution of mantle wedge oxygen fugacity during subduction initiation. Geology 43:775–778. https://doi.org/10.1130/G36742.1

Davis GA, Qian XL, Zheng YD (1996) Mesozonic deformation and plutonism in the Yunmengshan, a metamorphic core complex north of Beijing, China. In The tectonic evolution of Asia. Cambridge University Press, Cambridge, pp 253–279

Davis GA, Yadong Z, Cong W, Darby BJ, Changhou Z, Gehrels G (2001) Mesozoic tectonic evolution of the Yanshan fold and thrust belt, with emphasis on Hebei and Liaoning provinces, northern China. Mem Geol Soc Am 194:171–198

Evans KA (2012) The redox budget of subduction zones. Earth Sci Rev 113:11–32. https://doi.org/10.1016/j.earscirev.2012.03.003

Evans KA, Reddy SM, Tomkins AG, Crossley RJ, Frost BR (2017) Effects of geodynamic setting on the redox state of fluids released by subducted mantle lithosphere. Lithos 278:26–42. https://doi.org/10.1016/j.lithos.2016.12.023

Fan WM, Menzies M (1992) Destruction of aged lower lithosphere and accretion of asthenosphere mantle beneath eastern China. Geotecton Metallog 16:171–180

Frost DJ, McCammon CA (2008) The redox state of Earth's mantle. Annu Rev Earth Planet Sci 36:389–420

Gao S, Rudnick RL, Yuan HL, Liu XM (2004) Recycling lower continental crust in the North China craton. Nature 432:892

Gao YF, Santosh M, Hou ZQ, Wei RH, Ma GX, Chen ZK, Wu JL (2012) High Sr/Y magmas generated through crystal fractionation: evidence from Mesozoic volcanic rocks in the northern Taihang orogen. North China Craton Gondwana Res 22:152–168. https://doi.org/10.1016/j.gr.2011.11.002

Grocke SB, Cottrell E, de Silva S, Kelley KA (2016) The role of crustal and eruptive processes versus source variations in controlling the oxidation state of iron in Central Andean magmas. Earth Planet Sci Lett 440:92–104. https://doi.org/10.1016/j.epsl.2016.01.026

Harrison TM, Watson EB (1984) The behavior of apatite during crustal anatexis: equilibrium and kinetic considerations. Geochim Cosmochim Acta 48:1467–1477. https://doi.org/10.1016/0016-7037(84)90403-4

Jolivet L, Tamaki KK, Fournier M (1994) Japan Sea, opening history and mechanism: a synthesis. J Geophy Res: Solid Earth 99 (B11):22237–22259

Kelemen PB, Hanghøj K, Greene AR (2003) One view of the geochemistry of subduction-related magmatic arcs, with an emphasis on primitive andesite and lower crust. Treatise Geochem 3:593–659

Kelley KA, Cottrell E (2009) Water and the oxidation state of subduction zone magmas. Science 325:605–607

Kelley KA, Cottrell E (2012) The influence of magmatic differentiation on the oxidation state of Fe in a basaltic arc magma. Earth Planet Sci Lett 329–330:109–121. https://doi.org/10.1016/j.epsl.2012.02.010

Krishnamurthy P (2015) Modelling of magmatic and allied processes. J Geol Soc India 85:385. https://doi.org/10.1007/s12594-015-0228-1

Kusky TM, Windley BF, Wang L, Wang ZS, Li XY, Zhu PM (2014) Flat slab subduction, trench suction, and craton destruction: comparison of the North China, Wyoming, and Brazilian cratons. Tectonophysics 630:208–221

Lécuyer C, Ricard Y (1999) Long-term fluxes and budget of ferric iron: implication for the redox states of the Earth's mantle and atmosphere. Earth Planet Sci Lett 165:197–211. https://doi.org/10.1016/S0012-821X(98)00267-2

Lee CA, Leeman WP, Canil D, Li ZXA (2005) Similar V/Sc systematics in MORB and arc basalts: implications for the oxygen fugacities of their mantle source regions. J Petrol 46:2313–2336. https://doi.org/10.1093/petrology/egi056

Lee CA, Luffi P, Le Roux V, Dasgupta R, Albaréde F, Leeman WP (2010) The redox state of arc mantle using Zn/Fe systematics. Nature 468:681

Liang HY et al (2006) Zircon Ce^{4+}/Ce^{3+} ratios and ages for Yulong ore-bearing porphyries in eastern Tibet. Miner Depos 41:152

Ling MX et al (2009) Cretaceous ridge subduction along the lower yangtze river belt. East China Econ Geol 104:303–321

Ling MX, Wang FY, Ding X, Zhou JB, Sun WD (2011) Different origins of adakites from the Dabie Mountains and the Lower Yangtze River Belt, eastern China: geochemical constraints. Int Geol Rev 53:727–740. https://doi.org/10.1080/00206814.2010.482349

Ling MX et al (2013) Destruction of the North China Craton induced by ridge subductions. J Geol 121:197–213

Liu DY, Nutman AP, Compston W, Wu JS, Shen QH (1992) Remnants of ≥ 3800 Ma crust in the Chinese part of the Sino-Korean craton. Geology 20:339–342

Liu YS, Gao S, Kelemen PB, Xu W (2008) Recycled crust controls contrasting source compositions of Mesozoic and Cenozoic basalts in the North China Craton. Geochim Cosmochim Acta 72:2349–2376. https://doi.org/10.1016/j.gca.2008.02.018

Liu SA, Li SG, He YS, Huang F (2010) Geochemical contrasts between early Cretaceous ore-bearing and ore-barren high-Mg adakites in central-eastern China: implications for petrogenesis and Cu–Au mineralization. Geochim Cosmochim Acta 74:7160–7178. https://doi.org/10.1016/j.gca.2010.09.003

Liu J, Wang ZZ, Yu HR, Xia QK, Deloule E, Feng M (2017) Dynamic contribution of recycled components from the subducted Pacific slab: Oxygen isotopic composition of the basalts from 106 Ma to 60 Ma in North China Craton. J Geophys Res Solid Earth 122:988–1006. https://doi.org/10.1002/2016jb013156

Menzies MA, Fan WM, Zhang M (1993) Palaeozoic and Cenozoic lithoprobes and the loss of > 120 km of Archaean lithosphere, Sino-Korean craton, China. Geol Soc Lond Spec Publ 76:71–81. https://doi.org/10.1144/gsl.sp.1993.076.01.04

Menzies M, Xu Y, Zhang H, Fan W (2007) Integration of geology, geophysics and geochemistry: a key to understanding the North China Craton. Lithos 96:1–21. https://doi.org/10.1016/j.lithos.2006.09.008

Miles AJ, Graham CM, Hawkesworth CJ, Gillespie MR, Hinton RW, Bromiley GD (2014) Apatite: a new redox proxy for silicic magmas? Geochim Cosmochim Acta 132:101–119

Niu YL (2005) Generation and evolution of basaltic magmas: some basic concepts and a new on the origin of Mesozonic-Cenozoic basaltic volcanism in the Earstern China. Geol J China Univ 11:9–46

O'Neill HSC (1987) Quartz-fayalite-iron and quartz-fayalite-magnetite equilibria and the free energy of formation of fayalite (Fe_2SiO_4) and magnetite (Fe_3O_4). Am Mineral 72:67–75

Rielli A et al (2017) Evidence of sub-arc mantle oxidation by sulphur and carbon Geochemical. Perspectives 3:124–132

Sun SS, McDonough WF (1989) Chemical and isotopic systematics of oceanic basalts: implications for mantle composition and processes. Geol Soc Lond Special Publ 42:313–345. https://doi.org/10.1144/gsl.sp.1989.042.01.19

Sun WD, Ding X, Hu YH, Li XH (2007) The golden transformation of the Cretaceous plate subduction in the west Pacific. Earth Planet Sci Lett 262:533–542

Sun JF, Yang JH, Wu FY, Li X, Yang YP, Xie LW, Wilde SA (2010) Magma mixing controlling the origin of the Early Cretaceous Fangshan granitic pluton, North China Craton: in situ U-Pb age and Sr-, Nd-, Hf- and O-isotope evidence. Lithos 120:421–438. https://doi.org/10.1016/j.lithos.2010.09.002

Sun WD et al (2013) The link between reduced porphyry copper deposits and oxidized magmas. Geochim Cosmochim Acta 103:263–275

Sun WD et al (2015) Porphyry deposits and oxidized magmas. Ore Geol Rev 65:97–131

Sun WD, Li CY, Hao XL, Ling MX, Ireland T, Ding X, Fan WM (2016) Oceanic anoxic events, subduction style and molybdenum mineralization. Solid Earth Sci 1:64–73. https://doi.org/10.1016/j.sesci.2015.11.001

Sun SJ, Zhang LP, Zhang RQ, Ding X, Zhu HL, Zhang ZF, Sun WD (2018a) Mid-Late Cretaceous igneous activity in South China: the Qianjia example, Hainan Island. Int Geol Rev 60(11–14):1665–1683

Sun SJ, Ireland TR, Zhang LP, Zhang RQ, Zhang CC, Sun WD, (2018b) Palaeoarchaean materials in the Tibetan Plateau indicated by zircon. Int Geol Rev 60(8):1061–1072

Sun SJ, Yang XY, Wang GJ, Sun WD, Zhang H, Li CY, Ding X (2019) In situ elemental and Sr-O isotopic studies on apatite from the Xu-Huai intrusion at the southern margin of the North China Craton: Implications for petrogenesis and metallogeny. Chem Geol 510:200–214

Wang Q et al (2007) Early Cretaceous adakitic granites in the Northern Dabie Complex, central China: Implications for partial melting and delamination of thickened lower crust. Geochim Cosmochim Acta 71:2609–2636. https://doi.org/10.1016/j.gca.2007.03.008

Wang T et al (2012) Timing and processes of Late Mesozoic mid-lower-crustal extension in continental NE Asia and implications for the tectonic setting of the destruction of the North China Craton: mainly constrained by zircon U-Pb ages from metamorphic core complexes. Lithos 154:315–345

Wu FY, Sun DY, Li HM, Jahn BM, Wilde S (2002) A-type granites in northeastern China: age and geochemical constraints on their petrogenesis. Chem Geol 187:143–173. https://doi.org/10.1016/S0009-2541(02)00018-9

Wu FY, Lin JQ, Wilde SA, Zhang XO, Yang JH (2005a) Nature and significance of the Early Cretaceous giant igneous event in eastern China. Earth Planet Sci Lett 233:103–119

Wu FY, Yang JH, Wilde SA, Zhang XO (2005b) Geochronology, petrogenesis and tectonic implications of Jurassic granites in the Liaodong Peninsula, NE China. Chem Geol 221:127–156. https://doi.org/10.1016/j.chemgeo.2005.04.010

Wu K, Ling MX, Sun WD, Guo J, Zhang CC (2017) Major transition of continental basalts in the Early Cretaceous: implications for the destruction of the North China Craton. Chem Geol. https://doi.org/10.1016/j.chemgeo.2017.08.025

Xia QK, Liu J, Liu SC, Kovács I, Feng M, Dang L (2013) High water content in Mesozoic primitive basalts of the North China Craton and implications on the destruction of cratonic mantle lithosphere. Earth Planet Sci Lett 361:85–97

Xu YG (2001) Thermo-tectonic destruction of the archaean lithospheric keel beneath the sino-korean craton in china: evidence, timing and mechanism. Phys Chem Earth A Solid Earth Geod 26:747–757. https://doi.org/10.1016/S1464-1895(01)00124-7

Xu YG et al (2004) Crust-mantle interaction during the tectono-thermal reactivation of the North China Craton: constraints from SHRIMP zircon U-Pb chronology and geochemistry of Mesozoic plutons from western Shandong. Contrib Miner Petrol 147:750–767. https://doi.org/10.1007/s00410-004-0594-y

Xu HJ, Song YR, Ye K, Zhang JF, Wang HR (2012) Petrogenesis of mafic dykes and high-Mg adakitic enclaves in the Late Mesozoic Fangshan low-Mg adakitic pluton, North China Craton. J Asia Earth Sci 54–55:143–161

Yang JH, Wu FY, Wilde SA, Belousova E, Griffin WL (2008) Mesozoic decratonization of the North China block. Geology 36:467–470

Zhang HF, Sun M, Zhou XH, Fan WM, Zhai MG, Yin JF (2002) Mesozoic lithosphere destruction beneath the North China Craton: evidence from major-, trace-element and Sr-Nd-Pb isotope studies of Fangcheng basalts. Contrib Mineral Petrol 144:241–254

Zhang HF, Sun M, Zhou XH, Zhou MF, Fan WM, Zheng JP (2003) Secular evolution of the lithosphere beneath the eastern North China Craton: evidence from Mesozoic basalts and high-Mg andesites. Geochim Cosmochim Acta 67:4373–4387. https://doi.org/10.1016/S0016-7037(03)00377-6

Zhang H et al (2013) High oxygen fugacity and slab melting linked to Cu mineralization: evidence from dexing porphyry copper deposits, Southeastern China. J Geol 121:289–305. https://doi.org/10.1086/669975

Zhang CC, Sun WD, Wang JT, Zhang LP, Sun SJ, Wu K (2017) Oxygen fugacity and porphyry mineralization: a zircon perspective of Dexing porphyry Cu deposit, China. Geochim Cosmochim Acta 206:343–363

Zhao MT, Wang Y (2014) Geochemical characteristics and petrogenesis of the Shicheng diorite and Yunmengshan granite in Beijing area. Mineral Petrol 34:60–69

Zhao GC, Wilde SA, Cawood PA, Sun M (2001) Archean blocks and their boundaries in the North China Craton: lithological, geochemical, structural and P-T path constraints and tectonic evolution. Precambrian Res 107:45–73

Zhao DP, Maruyama S, Omori S (2007) Mantle dynamics of Western Pacific and East Asia: insight from seismic tomography and mineral physics. Gondwana Res 11:120–131. https://doi.org/10.1016/j.gr.2006.06.006

Zhao T, Zhu G, Lin S, Wang HJE-SR (2016) Indentation-induced tearing of a subducting continent: evidence from the Tan–Lu Fault Zone, East China. Earth Sci Rev 152:14–36

Zheng JP, Griffin WL, O'Reilly SY, Yu CM, Zhang H, Pearson N, Zhang M (2007) Mechanism and timing of lithospheric modification and replacement beneath the eastern North China Craton: peridotitic xenoliths from the 100 Ma Fuxin basalts and a regional synthesis. Geochim Cosmochim Acta 71:5203–5225. https://doi.org/10.1016/j.gca.2007.07.028

Zhu RX, Chen L, Wu FY, Liu JL (2011) Timing, scale and mechanism of the destruction of the North China Craton. Sci China Earth Sci 54:789–797. https://doi.org/10.1007/s11430-011-4203-4

Zhu RX, Yang JH, Wu FY (2012) Timing of destruction of the North China Craton. Lithos 149:51–60

Zhu G, Chen Y, Jiang DZ, Lin SZ (2015) Rapid change from compression to extension in the North China Craton during the Early Cretaceous: evidence from the Yunmengshan metamorphic core complex. Tectonophysics 656:91–110